BLACK HOLE MASS ESTIMATES AND EMISSION-LINE PROPERTIES OF A SAMPLE OF REDSHIFT $z > 6.5$ QUASARS*

Gisella De Rosa[1,2], Bram P. Venemans[3], Roberto Decarli[3], Mario Gennaro[4], Robert A. Simcoe[5], Matthias Dietrich[6], Bradley M. Peterson[1,2], Fabian Walter[3], Stephan Frank[1], Richard G. McMahon[7,8], Paul C. Hewett[7], Daniel J. Mortlock[9,10], and Chris Simpson[11]

[1] Department of Astronomy, The Ohio State University, 140 West 18th Avenue, Columbus, OH 43210, USA
[2] Center for Cosmology and AstroParticle Physics, The Ohio State University, 191 West Woodruff Avenue, Columbus, OH 43210, USA
[3] Max-Planck-Institut für Astronomie, Königstuhl 17, D-69117 Heidelberg, Germany
[4] Space Telescope Science Institute, 3700 San Martin Drive, Baltimore, MD 21218, USA
[5] MIT-Kavli Center for Astrophysics and Space Research, 77 Massachusetts Avenue, Cambridge, MA 02139, USA
[6] Department of Physics and Astronomy, Ohio University, Clippinger Lab 251B, Athens, OH 45701, USA
[7] Institute of Astronomy, University of Cambridge, Madingley Road, Cambridge CB3 0HA, UK
[8] Kavli Institute for Cosmology, University of Cambridge, Madingley Road, Cambridge CB3 0HA, UK
[9] Astrophysics Group, Imperial College London, Blackett Laboratory, Prince Consort Road, London, SW7 2AZ, UK
[10] Department of Mathematics, Imperial College London, London, SW7 2AZ, UK
[11] Astrophysics Research Institute, Liverpool John Moores University, Liverpool Science Park, 146 Brownlow Hill, Liverpool L3 5RF, UK

ABSTRACT

We present the analysis of optical and near-infrared spectra of the only four $z > 6.5$ quasars known to date, discovered in the UKIDSS-LAS and VISTA-VIKING surveys. Our data set consists of new Very Large Telescope/ X-Shooter and Magellan/FIRE observations. These are the best optical/NIR spectroscopic data that are likely to be obtained for the $z > 6.5$ sample using current 6–10 m facilities. We estimate the black hole (BH) mass, the Eddington ratio, and the Si IV/C IV, C III]/C IV, and Fe II/Mg II emission-line flux ratios. We perform spectral modeling using a procedure that allows us to derive a probability distribution for the continuum components and to obtain the quasar properties weighted upon the underlying distribution of continuum models. The $z > 6.5$ quasars show the same emission properties as their counterparts at lower redshifts. The $z > 6.5$ quasars host BHs with masses of $\sim 10^9 \, M_\odot$ that are accreting close to the Eddington luminosity ($\langle \log(L_{\rm Bol}/L_{\rm Edd}) \rangle = -0.4 \pm 0.2$), in agreement with what has been observed for a sample of $4.0 < z < 6.5$ quasars. By comparing the Si IV/C IV and C III]/C IV flux ratios with the results obtained from luminosity-matched samples at $z \sim 6$ and $2 \leqslant z \leqslant 4.5$, we find no evidence of evolution of the line ratios with cosmic time. We compare the measured Fe II/Mg II flux ratios with those obtained for a sample of $4.0 < z < 6.4$ sources. The two samples are analyzed using a consistent procedure. There is no evidence that the Fe II/Mg II flux ratio evolves between $z = 7$ and $z = 4$. Under the assumption that the Fe II/Mg II traces the Fe/Mg abundance ratio, this implies the presence of major episodes of chemical enrichment in the quasar hosts in the first ~ 0.8 Gyr after the Big Bang.

Key words: galaxies: high-redshift – quasars: emission lines

Online-only material: color figures

1. INTRODUCTION

In the past 10 yr, more than 60 quasars at $5.7 \lesssim z \lesssim 6.4$ have been discovered (e.g., Fan et al. 2006; Jiang et al. 2008, 2009; Venemans et al. 2007; Willott et al. 2007, 2010; Morganson et al. 2012,; Bañados et al. 2014), mainly thanks to optical surveys such as the Sloan Digital Sky Survey (SDSS; York et al. 2000), the Canada France High-z Quasar Survey (Willott et al. 2007), and the Panoramic Survey Telescope and Rapid Response System Survey 1 (Kaiser et al. 2010). Only four quasars are known to date at $z > 6.5$: ULAS J112001.48+064124.3 (hereafter J1120+0641) at $z = 7.1$, discovered by Mortlock et al. (2011) in the Unite Kingdom Infrared Deep Sky Survey (UKIDSS) Large Area Survey (LAS; Lawrence et al. 2007); and VIKING J234833.34–305410.0 (hereafter J2348–3054) at $z = 6.9$, VIKING J010953.13–304726.3 (hereafter J0109–3040) at $z = 6.7$, and VIKING J030516.92–315056.0 (hereafter J0305–3150) at $z = 6.6$, recently discovered by Venemans

et al. (2013) in the Visible and Infrared Survey Telescope for Astronomy (VISTA) Kilo-Degree Infrared Galaxy (VIKING; Arnaboldi et al. 2007) survey. These very high redshift quasars are direct probes of the universe less than 1 Gyr after the Big Bang. They are fundamental in studying the physical conditions of the universe during the epoch of reionization (e.g., Bolton et al. 2011; Mortlock et al. 2011; Simcoe et al. 2012), the formation and early growth of supermassive black holes (SMBHs; e.g., Volonteri 2010; Latif et al. 2013), the galaxy formation processes (e.g., Walter et al. 2009; Wang et al. 2013), and the interstellar medium chemical evolution (e.g., Jiang et al. 2007; Simcoe et al. 2011, 2012).

The bright emission lines in the rest-frame UV spectrum of quasars ($\lambda_{\rm rest} \sim 1000$–3000 Å) provide insights on the properties of the black hole (BH) and of the circumnuclear gas. For example, one can use the Doppler emission-line widths to estimate the mass of the BH ($M_{\rm BH}$) via empirical mass-scaling relations (e.g., Vestergaard & Peterson 2006; Vestergaard & Osmer 2009). At the same time, photoionization models show that various emission-line flux ratios (e.g., N III]/O III], N V/(C IV+O IV), and N V/He II) can be used to derive chemical abundances of the broad line region (BLR) gas (e.g., Hamann et al. 2002;

Nagao et al. 2006) and, thus, to set constraints on the star formation history of the quasar host galaxy. In particular, the abundance of Fe versus α elements (e.g., Mg and O that are produced via α processes) represents a key factor in understanding the chemical evolution of galaxies in the early universe. According to chemical evolution scenarios, the dominant source of iron (Fe) is the explosion of type Ia supernovae (SNe Ia), that are thought to originate from intermediate-mass stars in close binary systems and are characterized by long lifetimes ($\sim$1 Gyr after the onset of star formation, e.g., Tinsley 1979; Matteucci & Greggio 1986). On the other hand, α elements are assumed to be mainly produced by core collapse supernovae (SNe of types II, Ib, and Ic), that originate from more massive stars which explode shortly after the initial starburst ($\sim$8 Myr). The amount of Fe returned to the interstellar medium through SN II ejecta is rather low (Yoshi et al. 1996). Therefore, the Fe/α ratio is expected to be a strong function of age in young systems, with the Fe enrichment being typically delayed of $\sim$1 Gyr. However this delay can be much shorter ($\sim$0.3 Gyr) for massive elliptical galaxies (e.g., Matteucci & Recchi 2001; Pipino et al. 2011).

Numerous spectroscopic studies of high-redshift quasars (e.g., Jiang et al. 2007; Kurk et al. 2007, 2009; De Rosa et al. 2011; Willott et al. 2010) have shown that high-redshift quasars host BHs with $M_{\rm BH} \sim 10^9 \, M_\odot$ that are accreting close to the Eddington limit. In particular, from the consistent analysis of a sample of 22 sources with $4.0 < z < 6.5$, De Rosa et al. (2011) found that, at a given luminosity, the $z > 4$ sources are accreting faster than those at low redshift (see also Trakhtenbrot et al. 2011). The average Eddington ratio for the high-redshift quasar population is $\langle \log(L_{\rm Bol}/L_{\rm Edd}) \rangle = -0.35 \pm 0.25$, while for a luminosity-matched sample at $0.35 < z < 2.25$ the average Eddington ratio is $\langle \log(L_{\rm Bol}/L_{\rm Edd}) \rangle = -0.80 \pm 0.24$. At the same time, Mortlock et al. (2011) estimated a BH mass of $M_{\rm BH} = 2.0^{+1.5}_{-0.7} \times 10^9 \, M_\odot$ for J1120+0641, and a corresponding Eddington ratio of $L_{\rm Bol}/L_{\rm Edd} \sim 1.2^{+0.6}_{-0.5}$. The presence of quasars hosting BHs with masses $\gtrsim 10^9 \, M_\odot$ when the universe is less than 1 Gyr old challenges models of BH seed formation (e.g., Volonteri 2010; Latif et al. 2013).

At low redshift, elemental abundances estimated from both emission and intrinsic absorption lines show that quasar environments are characterized by solar or super-solar metallicities. Jiang et al. (2007) estimated the BLR metallicity for a sample of six luminous quasars with $5.8 < z < 6.3$ and found super solar metallicities (typical value of $\sim$4 $Z_\odot$) and no strong evolution in metallicity up to $z \sim 6$. The observational proxy that is usually adopted to trace the Fe/Mg abundance ratio is the Fe II/Mg II line ratio. For $z > 5.7$ quasars the Mg II emission line and the strong Fe II complexes are redshifted in the NIR. Previous NIR-spectroscopy works that studied the Fe II/Mg II line ratio in samples including high-z quasars (e.g., Barth et al. 2003; Dietrich et al. 2003; Iwamuro et al. 2004; Jiang et al. 2007; Kurk et al. 2007) showed an increase in the scatter of the measured Fe II/Mg II line ratios at $z \sim 6$. However, by performing a consistent analysis of a sample of 22 qgeasars with $4.0 < z < 6.5$, that included many of the sources analyzed in previous studies, De Rosa et al. (2011) found no sign of evolution in the Fe II/Mg II line ratio for $4.0 < z < 6.5$, suggesting an early chemical enrichment of the circumnuclear gas.

The goal of this paper is to characterize the BH masses and the emission properties of the only four quasars known to date at $z > 6.5$. We present new spectroscopic data for J1120+0641; observations were carried with the X-Shooter spectrograph (Vernet et al. 2011) mounted on the Very Large Telescope (VLT). Together with the new data, we analyze all the observations of the $z > 6.5$ sources collected by our group using the VLT/X-Shooter spectrograph and the Folded-port InfraRed Echellette spectrograph (FIRE; Simcoe et al. 2013) mounted on the Magellan Telescope. The paper is structured as follows. In Section 2, we describe the observations and the data reduction. In Section 3, we discuss our spectral decomposition and the modeling procedure, while in Section 4, we present the results and discuss their implications. Finally, we give a brief summary in Section 5. We assume the following ΛCDM cosmology throughout the paper: $H_0 = 70 \, {\rm km \, s^{-1} \, Mpc^{-1}}$, $\Omega_M = 0.28$, and $\Omega_\Lambda = 0.72$ (Komatsu et al. 2011).

2. DATA

Our sample consists of the only four quasars known to date with $z > 6.5$: J1120+0641, J2348$-$3054, J0109$-$3047, and J0305$-$3150. Their absolute magnitudes range between $-26.6 < M_{\rm 1450, AB} < -25.6$ (see Table 1 for details).

2.1. Observations and Data Reduction

We present new X-Shooter data for J1120+0641: observations were carried out between 2011 March and May (total exposure time 18,000 s). X-Shooter is a medium resolution Echellette spectrograph mounted on the Cassegrain focus of the 8.2 m VLT Kuyen telescope (UT2). X-Shooter covers three wavelength regions with three different spectrographs: UVB arm 3000–5595 Å, VIS arm 5595–10240 Å, and NIR arm 10240–24800 Å. Given the high redshift of the source, the rest-frame UV emission lines are redshifted at $\lambda_{\rm obs} \gtrsim 10000$ Å. At the same time the Gunn–Peterson absorption (Gunn & Peterson 1965) of the Ly continuum entirely suppresses the flux at wavelengths $\lambda_{\rm obs} < 912 \, (1 + z)$ Å ~ 7500 Å. Therefore we focus only on the VIS and NIR parts of the spectrum. We used the $0\farcs9 \times 11''$ slit for both VIS and NIR observations (pixel scales equal to $0\farcs16$ pixel^{-1} and $0\farcs21$ pixel^{-1}, respectively), while the DIMM seeing varied between $0\farcs6$ and $1\farcs7$. The resulting spectra have a resolution $R = 8800$ in the VIS bands and $R = 5300$ in the NIR. The raw two-dimensional spectra were rectified and wavelength calibrated by using the X-Shooter pipeline version 1.3.7 (Modigliani et al. 2010). Extraction and flux calibration using spectrophotometric standard stars were instead performed by using customized IDL routines. The final absolute flux calibration was obtained by matching the one-dimensional spectra to the observed UKIDSS infrared flux. UKIDSS data were collected between 2010 November and 2011 January. Our X-Shooter pipeline produces four separated spectral segments covering 8500–10200 Å, 10000–14200 Å, 14000–18200 Å, and 18000–24000 Å. After properly degrading the orders with higher resolution (bluer orders) to the lower resolution of the redder orders, individual segments were merged together by computing an inverse variance weighted average in the overlapping regions.

Together with the new data, we analyzed all the observations of the $z > 6.5$ sources that our group collected during 2011 and 2012. X-Shooter observations of J2348$-$3054 (total exposure time 8738 s) and of J0109$-$3047 (total exposure time 21,600 s) were carried out in 2011 August and November. The resolution of the spectra varies between $R = 5400$–8800 in the VIS bands and between $R = 4000$–5000 in the NIR ones. A detailed description of observing settings and data reduction can be found in the discovery paper (Venemans et al. 2013). Observations of J0305$-$3150 (total exposure time of 26,400 s)

Table 1
Quasars in Current Sample

Quasar Name	R.A. (J2000)	Decl. (J2000)	z	$M_{1450,\mathrm{AB}}$	A_V	Spectrograph
J1120+0641	$11^h20^m01\overset{s}{.}48$	$+06°41'24\overset{''}{.}3$	7.1	-26.6 ± 0.1	0.1601	X-Shooter, FIRE
J2348–3054	$23^h48^m33\overset{s}{.}34$	$-30°54'10\overset{''}{.}0$	6.9	-25.72 ± 0.14	0.0408	X-Shooter
J0109–3047	$01^h09^m53\overset{s}{.}13$	$-30°47'26\overset{''}{.}3$	6.7	-25.52 ± 0.15	0.0669	X-Shooter
J0305–3150	$03^h05^m16\overset{s}{.}92$	$-31°50'56\overset{''}{.}0$	6.6	-25.96 ± 0.06	0.0381	FIRE

and J1120+0641 (total exposure time of 54,036 s) were carried out with the FIRE spectrograph mounted on the Magellan/Baade 6.5 m telescope. The data were taken with a 0″.6 slit, resulting in a spectral resolution of $R = 6000$ over the full 8200 Å–25100 Å wavelength range. A detailed description of observing conditions and data reduction can be found in Venemans et al. (2013) for J0305–3150 and in Simcoe et al. (2012) for J1120+0641.

2.2. Post-processing

In order to homogenize the spectral resolutions and increase the signal to noise ratio S/N per resolution element, we first smoothed the reduced spectra by convolving them with a Gaussian kernel with FWHM $= 100\,\mathrm{km\,s^{-1}}$ ($\sigma_{\mathrm{kernel}} \sim 45\,\mathrm{km\,s^{-1}}$). We then re-sampled the spectra in velocity space by selecting one representative element every $\Delta v \sim 3\,\sigma_{\mathrm{kernel}}$. Errors on the smoothed spectra were computed from the errors on the extracted spectra via standard error propagation. The smoothing and resampling do not affect our results since we are interested in studying the continuum and broad emission line (BEL) properties (typical BEL rest-frame $\sigma_{\mathrm{line}} > 1000\,\mathrm{km\,s^{-1}}$). The spectra were further corrected for Galactic extinction using the Cardelli et al. (1989) law and A_V values obtained from the extinction map by Schlegel et al. (1998) (assuming $R_V = 3.1$, see Table 1).

For J1120+0641 data were collected with both X-Shooter and FIRE. The two reduced spectra present different spectral shapes (see Figure 1, top panel), with a clear disagreement between the spectral slopes at both $\lambda_{\mathrm{obs}} < 11000$ Å and $\lambda_{\mathrm{obs}} > 20000$ Å. Since the detected differences in the spectral shape could be driven by a variety of different causes involving both observations and data reduction (e.g., slit losses, telluric absorption correction, inter-order flux losses), we further compared the spectra with the lower resolution spectrum ($R \sim 500$) of the same source obtained with the Gemini near-infrared spectrograph (GNIRS), published by Mortlock et al. (2011) (see Figure 1, top panel). GNIRS is a cross-dispersed spectrograph mounted on the Gemini North Telescope. In Figure 1 we show the flux ratios between the GNIRS and X-Shooter spectra (central panel), and between those obtained with GNIRS and FIRE (we also plot the wavelength ranges of individual orders of X-Shooter and FIRE for reference).

The X-Shooter spectral shape is overall in good agreement with the GNIRS data, with the exception of two regions: the Lyα region (Y-band) and the Mg II region (K-band). While the Y-band issues are most probably related to uncertainties in the absolute flux calibration (the Y-band light is measured in part in the VIS arm and in part in the NIR arm), the K-band issues are due to vignetting affecting the redder orders of the NIR arm.

For the FIRE spectrum, a disagreement with the GNIRS spectral shape is noticeable, with the difference between the two spectra slowly increasing toward blue wavelengths and reaching ~15% in the Y-band. While the differential effect might point toward slit losses, we could not unequivocally iden-
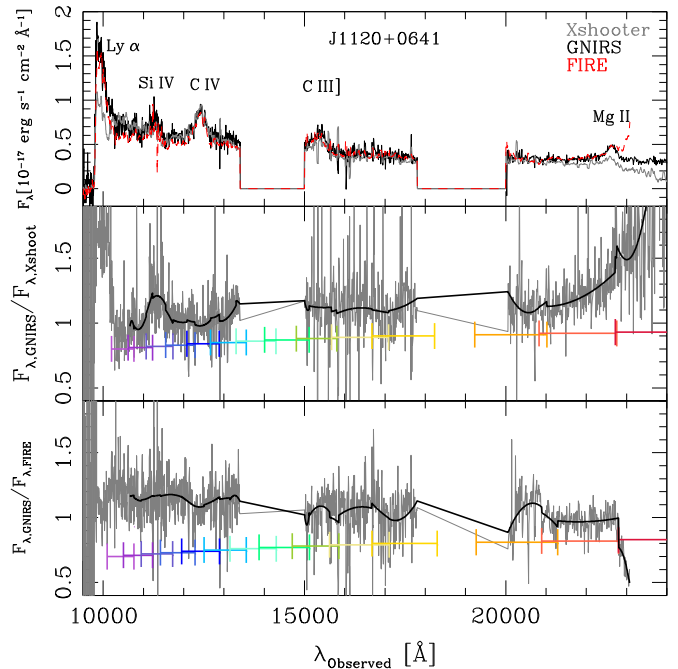

Figure 1. Comparison of the spectroscopic observations of J1120+0641—Top panel: X-Shooter (gray solid line), FIRE (red dashed line) and GNIRS data (black solid line). Middle and bottom panels: ratio between the GNIRS and the X-Shooter and FIRE spectra (gray dashed line). We have obtained a second-order flux calibration for the echellette spectra under the assumption that the GNIRS flux calibration is correct (see the text). We have fitted the flux ratio in each echellette order (colored segment) with a second-order polynomial (black solid line). In case of overlapping orders the final correction is the weighted mean of the individual spectral orders. This second-order flux calibration correction can be performed only for J1120+0641, since this is the only source for which we have non-Echellette data.

(A color version of this figure is available in the online journal.)

tify the cause of the issues. In addition to the inconsistencies which vary slowly across the Y- to K-bands, the FIRE and X-Shooter data both exhibit order-to-order residuals in the flux ratio, characteristic of varying S/N across the echelle blaze in each order. Since the low resolution GNIRS spectrum was obtained by adding only five different orders (which reduces significantly the fraction of spectrum that may be affected by inter-order flux losses) and given the overall good agreement between the GNIRS and X-Shooter spectra, we decided to assume the GNIRS spectrum to be the best available representation of the source intrinsic spectrum. We were then able to compute a second-order flux calibration correction for both the X-Shooter and FIRE spectra. We excluded spectral regions that were significantly contaminated by telluric absorption (13500 Å $< \lambda_{\mathrm{obs}} <$ 15000 Å, 17800 Å $< \lambda_{\mathrm{obs}} <$ 20000 Å) and the Lyα region from the computation, given the higher uncertainties in the flux calibration of the X-Shooter data. For each spectral order, we fitted the $F_{\lambda,\mathrm{GNIRS}}/F_{\lambda,\mathrm{X\text{-}Shooter,FIRE}}$ flux ratio with a second-order polynomial. For overlapping orders,
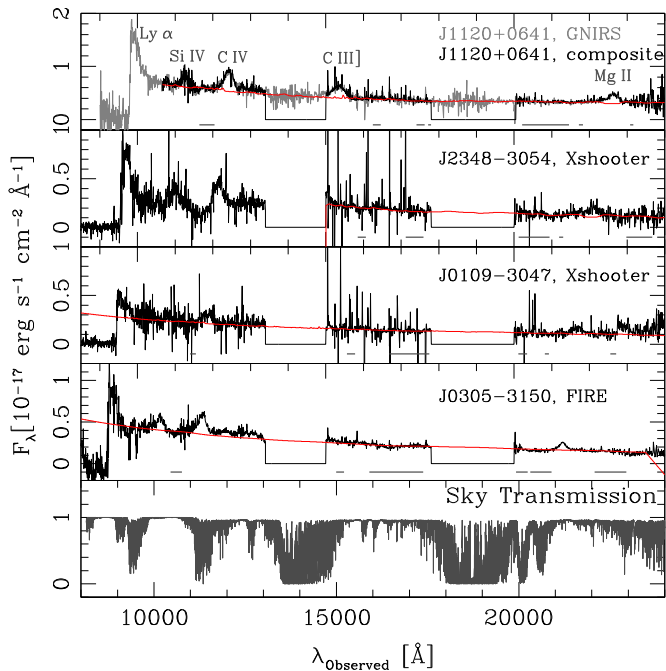
Figure 2. Final optical-to-NIR spectra of all $z > 6.5$ quasars. Black solid line: observed quasar spectra corrected for Galactic reddening. For J1120+0641 we plot the composite spectrum obtained from the combination of X-Shooter and FIRE data, after secondary flux correction (gray solid line: GNIRS spectrum). Red solid line: "best-fit" continuum model. For J2348−3054 (BAL quasar) we limit our spectral decomposition to $\lambda_{\rm obs} \geqslant 15000$ Å. Dark gray segments: continuum modeling windows. Bottom panel: Paranal sky transmission spectrum (nominal airmass = 1).

(A color version of this figure is available in the online journal.)

the final correction was computed as the weighted mean of the individual ones. After applying the second-order flux calibration corrections, we created a "final" J1120+0641 high S/N spectrum by computing the weighted mean of the FIRE and X-Shooter spectra.

It was not possible to compute second-order flux calibration corrections for J2348−3054, J0109−3047, and J0305−3150 since non-echellette lower resolution spectra are not available. By multiplying the observed spectra by the VIKING-VISTA filter throughput curves though, we were able to compare the broadband magnitudes obtained from the spectra (flux calibrated via the spectro-photometric standards) with the catalog ones. For both the X-Shooter spectra (J2348−3054 and J0109−3047) the derived $Y − J$ color is 0.2 mag redder than the broad–band catalog colors. For J0305–3150 instead, the observed $Y − J$ color is in agreement with the catalog one. The final spectra are shown in Figure 2.

3. DATA ANALYSIS

We focus on the rest-frame UV spectral region with 1280 Å $< \lambda_{\rm rest} < 3000$ Å. This wavelength range is characterized by the presence of strong BELs such as Si IV + O IV] $\lambda\lambda1397, 1402$, C IV $\lambda1549$, C III] $\lambda1908$, and Mg II $\lambda2798$, the non-stellar nuclear continuum, the Balmer continuum and the Fe II and Fe III emission-line blends. The last three emission features overlap in the spectral range of interest and constitute our underlying "pseudo-continuum." We excluded from the analysis spectral regions that are significantly contaminated by telluric absorption (13500 Å $< \lambda_{\rm obs} < 15000$ Å, 17800 Å $< \lambda_{\rm obs} < 20000$ Å) and the Lyα region (given the uncertainties that might affect the flux

calibration). For J2348−3054, we were forced instead to limit our analysis to $\lambda_{\rm obs} > 15000$ Å: this source is a broad absorption line (BAL) quasar (see also Venemans et al. 2013), hence all the spectral regions suitable for continuum modeling at 10000 Å $< \lambda_{\rm obs} < 15000$ Å are affected by absorption.

3.1. Spectral Model

3.1.1. Continuum Components

We modeled the pseudo-continuum with the following components.

1. *Non-stellar Continuum Emission.* The dominant component of a quasar spectrum at rest-frame UV–optical wavelengths is the non-stellar nuclear continuum, modeled as a power law:

$$F_{\lambda,\rm PL} = F_{0,\rm PL} \left(\frac{\lambda}{1000\,\text{Å}} \right)^{\alpha}. \qquad (1)$$

The determination of the slope coefficient α depends on both the fitting procedure and the observed spectral range. In the literature, in case of wide wavelength coverage, the fit of the power law is usually performed by selecting narrow fitting windows free of any contribution by other emission components. In this work however, in order to increase the width of the fitting windows and to reduce possible biases due to residual contamination from other emission features, we model the power-law component simultaneously with the Balmer continuum and with the Fe II emission-line forest. This allows us to adopt broader continuum fitting windows (see Figure 2). Lower redshift SDSS quasars ($z < 3$) have a typical power-law slope of $\alpha \sim -1.3$, but the exact value can vary significantly from source to source. Decarli et al. (2010), for example, analyzed a sample of 96 quasars at $z < 3$ and obtained a mean value of $\alpha = -1.3$ with a 1σ dispersion of 1.6. De Rosa et al. (2011) analyzed a sample of 22 high-redshift quasars ($4.0 < z < 6.5$) with NIR spectral coverage (2000 Å $\lesssim \lambda_{\rm rest} \lesssim 3000$ Å) and found a consistent mean value of $\alpha = -1.5$ with a 1σ dispersion of 1.2.

2. *Balmer Continuum Emission.* We assume gas clouds with uniform temperature $T_{\rm e}$, that are partially optically thick. In this case, for wavelengths bluer than the Balmer edge ($\lambda_{\rm BE} = 3646$ Å, rest frame), the Balmer spectrum can be parameterized as (Grandi 1982; Wills et al. 1985)

$$F_\lambda = F_{\rm BE}\, B_\lambda(T_{\rm e})\, (1 - e^{-\tau_{\rm BE}(\lambda/\lambda_{\rm BE})^3}),\ \lambda < \lambda_{\rm BE}, \qquad (2)$$

where $B_\lambda(T_{\rm e})$ is the Planck function at the electron temperature $T_{\rm e}$, $\tau_{\rm BE}$ is the optical depth at the Balmer edge, and $F_{\rm BE}$ is the normalized flux density at the Balmer edge. We have used the library of Balmer continuum emission templates created by Dietrich et al. (2003). The library includes 16 Balmer continuum templates probing different values of the (1) electron temperature ($T_{\rm e} = 10,000, 125,00, 15,000, 20,000$ K) and (2) optical depth at the Balmer edge ($\tau_{\rm BE} = 0.1, 0.5, 1, 2$). We consider each template as a fixed point in our multidimensional grid and evaluate the template likelihood as a function of the template normalization, $F_{0,\rm BC}$, i.e.,

$$F_{\lambda,\rm BC} = F_{0,\rm BC}\, F_{\rm template,BC}(T_{\rm e}, \tau_{\rm BE}). \qquad (3)$$

3. *Fe II and Fe III Emission Lines.* The Fe II and Fe III ions emit a forest of lines, many of which are blended. We model the Fe II + Fe III emission in our quasar spectra using a scaled and broadened version of the empirical emission template spectrum of Vestergaard & Wilkes ([2001](#)). This template is based on the high resolution spectrum of the narrow line Seyfert 1 galaxy PG0050+124 ($z = 0.061$), observed with the *Hubble Space Telescope*. Vestergaard & Wilkes isolated the emission-line template by fitting and subtracting the power-law continuum and the absorption emission features from all the elements but Fe. Since we are mainly interested in the Fe II/Mg II flux ratio, we model the continuum on windows characterized by Fe II complexes only. The intrinsic broadness of the Fe II component, σ_{QSO}, is unknown and varies from quasar to quasar, therefore we have created a library of Fe II + Fe III templates by convolving the original template in velocity space with a Gaussian kernel with

$$\sigma = \sqrt{FWHM_{QSO}^2 - FWHM_{Templ}^2}/2\ln(2\sqrt{2}), \quad (4)$$

where $FWHM_{Templ}$ is the characteristic FWHM of iron features in the spectrum of PG0050+124, and the final FWHM of the iron features in the quasar spectrum varies between $FWHM_{QSO} = (1000–16,000)\,km\,s^{-1}$, in steps of $500\,km\,s^{-1}$. We consider each template as a fixed point in our multidimensional grid and evaluate the template likelihood as a function of the template normalization, $F_{0,Fe}$,

$$F_{\lambda,Fe} = F_{0,Fe}\, Fe_{\,Templ}(\sigma). \quad (5)$$

3.1.2. Emission-line cComponents

In low S/N regimes (average continuum S/N per pixel $\lesssim 10$), details of the emission-line profiles are not discernible, but we find that the emission lines can be well modeled by simple Gaussian functions,

$$F_{\lambda,G} = F_{0,G}\exp\left(\frac{(\lambda - \lambda_0)^2}{2\sigma^2}\right), \quad (6)$$

where the line amplitude $F_{0,G}$, the line dispersion σ and the peak wavelength λ_0 are the model parameters. At higher S/N (average continuum S/N per pixel $\gtrsim 10$) the level of detectable details in the line shape improves significantly: emission lines often present asymmetric profiles characterized by prominent red and/or blue wings, and various degrees of kurtosis. Therefore, in high S/N regimes, the simple Gaussian description often becomes unsatisfactory. In cases where the emission line is similar to a Gaussian but asymmetric, van der Marel & Franx ([1993](#)) show that the line can be well described by a particular subset of Gauss–Hermite polynomials of fourth degree (see also Riffel [2010](#))

$$F_{\lambda,GH} = F_{0,GH}\frac{e^{-w^2/2}}{\sigma\sqrt{2\pi}}[1 + h_3 H_3(w) + h_4 H_4(w)], \quad (7)$$

where $F_{0,GH}$ is the amplitude of the Gauss–Hermite series, $w = (\lambda - \lambda_0)/\sigma$, h_j are the Gauss–Hermite moments and the Hermite polynomials $H_j(w)$ are, respectively,

$$H_3(w) = \frac{1}{\sqrt{6}}(2\sqrt{2}w^3 - 3\sqrt{2}w) \quad (8)$$

and

$$H_4(w) = \frac{1}{\sqrt{24}}(4w^4 - 12w^2 + 3). \quad (9)$$

The h_3 Gauss–Hermite moment represents the degree of asymmetry with respect to a Gaussian profile, while the h_4 moment assesses the degree of kurtosis or "peakiness" of the line ($h_4 > 0$: profile more boxy than Gaussian profile; $h_4 < 0$: profile more peaky than Gaussian profile). In case $h_3 = h_4 = 0$ $F_{\lambda,GH}$ is equal to a simple Gaussian profile. We fitted each of the detected bright emission lines (Si IV, C III], C IV, and Mg II) with a Gaussian profile for the sources characterized by a continuum S/N $\lesssim 10$ (J0109-3047 and J2348–3054) and with a Gauss–Hermite polynomial for the remaining sources (J1120+0641 and J0305–3150). Note that, given the spectral quality and the final resolution of our spectra:

1. The individual transitions of O IV] and the Si IV, C IV, and Mg II doublets are blended. Therefore we did not attempt to isolate their individual components (see also Jiang et al. [2007](#));

2. we ignored Al III λ1857 and Si III] λ1892 emission lines that are blended with the strong C III] emission since the latter is typically significantly brighter (e.g., Vanden Berk et al. [2001](#)); and

3. we did not attempt to model any narrow emission-line component, since it is not possible to reliable subtracting them in presence of strong BELs without unblended templates for the velocity widths (that do not exist, e.g., Denney et al. [2014](#)).

3.2. Spectral Modeling

We perform the spectral modeling in the source rest frame. For high-redshift quasars, it is possible to obtain a direct estimate of the systemic redshift through the detection of cold molecular gas phase in the host galaxy (e.g., Walter et al. [2003](#); Wang et al. [2010](#); Venemans et al. [2012](#)). Venemans et al. ([2012](#)) observed the [C II] λ158 μm emission line for J1120+0641 and measured a systemic redshift $z_{[C II]} = 7.0842 \pm 0.0004$, which is in agreement with the redshift estimate obtained by Mortlock et al. ([2011](#), $z = 7.085 \pm 0.003$) from the cross-correlation of the observed Mg II emission line with the quasar composite spectrum of Hewett & Wild ([2010](#)). Therefore, for J1120+0641, we fixed the systemic redshift to the $z_{[C II]}$ estimate. For J0305–3150, J0109–3047, and J2348–3054 there are no available observations of the cold molecular gas phase. Therefore, for these objects, we assume that the Mg II emission line (which is a low ionization line) as a proxy of the quasar systemic redshift (see also Jiang et al. [2007](#); Kurk et al. [2007](#); De Rosa et al. [2011](#)). Low-ionization lines are preferred to high-ionization lines (e.g., C IV) because the latter can present high-velocity offsets with respect to the source systemic redshift ($\Delta v \gtrsim 1000\,km\,s^{-1}$, corresponding to $\Delta z \sim 0.02$ at $z \sim 6$, see, e.g., Richards et al. [2002](#), [2011](#); Shang et al. [2007](#) and references therein). Hence, for the VIKING quasars, we assumed as initial guess for the systemic redshift the one obtained from the onset of the Lyα Gunn–Peterson absorption (Venemans et al. [2013](#)). The initial guess was then substituted by $z_{Mg II}$, and both continuum and line modeling were iteratively performed till the convergence on $z_{Mg II}$ was reached.

The modeling of the continuum is performed following a grid-based approach. Given the continuum model,

$$F_{\lambda,Model} = F_{\lambda,PL} + F_{\lambda,BC} + F_{\lambda,Fe}, \quad (10)$$

we computed the likelihood of the data in the spectral regions that show only continuum and Fe II emission ($d_{\rm cont}$) given the model parameters (Θ) as $P(d_{\rm cont}|\Theta) = Ne^{-\chi^2/2}$, where N ensures that the likelihood is normalized. In the likelihood definition, we have

$$\chi^2 = \sum_i \frac{(F_{\lambda,{\rm obs},i} - F_{\lambda,{\rm Model},i})^2}{\sigma_i^2}, \qquad (11)$$

where $F_{\lambda\,{\rm obs},i}$ is the observed flux, σ is the uncertainty on the observed flux and the index i runs over the pixels that present only continuum and Fe II emission. This definition of the likelihood assumes that the uncertainty on the flux in individual pixels is Gaussian.

Using a 3σ clipping algorithm, we automatically excluded noise peaks and residuals from telluric absorption correction from our fitting windows. There are six model parameters Θ: power-law normalization and slope, Balmer continuum normalization and template identifier, iron template normalization and identifier. All the parameters, with the exception of the Balmer continuum and iron template identifiers, where discretized over a regular grid. The parameter ranges were chosen to ensure that each of the marginal probability distributions goes to zero at the boundaries of the probed interval. We assumed priors that are uniform over the specified domain for Θ, and zero elsewhere. This implies that, within the domain, the posterior probability distribution function (pdf) is proportional to the likelihood, $P(\Theta|d_{\rm cont}) \propto P(d_{\rm cont}|\Theta)$. The resolution of the individual grid was chosen and adapted in order to properly sample the peak of the posterior distribution. Hereafter we indicate the continuum model with the maximum posterior pdf (or maximum likelihood) as the "best-fit" continuum model.

To derive the emission-line properties we assumed either a Gaussian or a Gauss–Hermite line profile (see Section 4.2). We indicate the set of unknown parameters of a line with Λ. After subtracting the "best-fit" continuum model, we derived Λ using a χ^2 minimization routine. We then measured the line FWHM and dispersion (following Peterson et al. 2004), the wavelength corresponding to the line peak ($\lambda_{\rm Peak}$), the line flux, and the equivalent width (EW) directly from the line model. We adopted the corresponding values as "best-fit" estimates of the line properties.

The vast majority of the studies in the literature do not take into account the errors on the emission-line properties that result from the uncertainties of the continuum modeling. This is particularly important when the S/N of the spectra is poor and degeneracies among the model components are present. For these reasons, we estimated the errors on the line properties in two distinct steps. First, we estimated the uncertainty on Λ, given the posterior distribution of the continuum parameters, $P(\Theta|d_{\rm cont})$. This accounts for the impact of potential degeneracies in the continuum parameters. Second, we estimated the uncertainty due to the S/N of the line, for a fixed continuum model (fixed Θ).

In the first step, we sampled Θ from $P(\Theta|d_{\rm cont})$ with a Monte Carlo rejection method. For each sample we subtracted the corresponding continuum model. We then restricted the analysis to the continuum subtracted data within a line-fitting spectral region ($d_{\rm line}$) to obtain the estimated line properties from the χ^2 minimization routine ($\Lambda_{\rm best-fit}(\Theta)$). This is equivalent to obtaining the pdf of the line properties, $P(\Lambda|d_{\rm line})$, marginalized
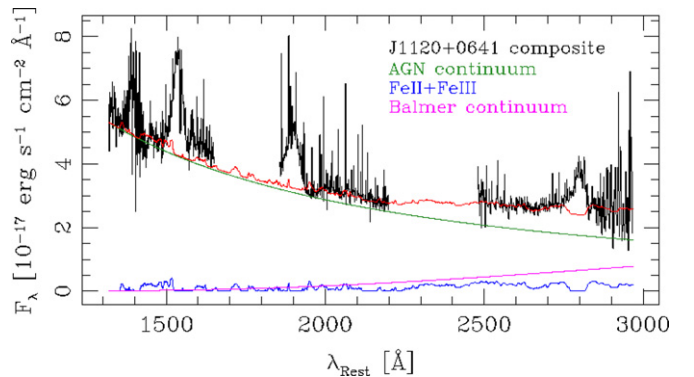

Figure 3. Continuum spectral decomposition for J1120+0641: AGN continuum (green), Balmer continuum (magenta), Fe II + Fe III line forest (blue), pseudo-continuum "best-fit" model (red) corresponding to the sum of the AGN continuum, the Balmer continuum, and the Fe II + Fe III line forest.

(A color version of this figure is available in the online journal.)

over the distribution of the continuum models

$$P_\delta(\Lambda|d_{\rm line}) = \int \delta(\Lambda - \Lambda_{\rm best-fit}(\Theta))\, P(\Theta|d_{\rm cont})d\Theta, \qquad (12)$$

under the assumption that $P(\Lambda|\Theta, d_{\rm line})$ is a Dirac's δ function centered on the line best-fit properties, i.e., $P(\Lambda|\Theta, d_{\rm line}) = \delta(\Lambda - \Lambda_{\rm best-fit}(\Theta))$. One can think of $P_\delta(\Lambda|d_{\rm line})$ as a weighted mean of the best-fit line properties at fixed Θ, with weights proportional to $P(\Theta|d_{\rm cont})$.

However, for a given continuum model (for given Θ), the line property estimates are significantly affected by sources of error that depend not only on the overall S/N of the data, but also on the assumed line profile, on intrinsic absorption lines and on telluric contamination. This means that $P(\Lambda|\Theta, d_{\rm line})$ is not a δ function.

The second step of our error estimate consists in evaluating the spread of $P(\Lambda|\Theta, d_{\rm line})$. To do so, we followed Assef et al. (2012) and used a Monte Carlo approach. Starting from the line best-fit model and from the measured flux uncertainty, we generated 5000 resampled spectra where the flux in each pixel was randomly drawn from a Gaussian distribution with mean value equal to the best-fit model flux and dispersion equal to the flux uncertainty. By re-measuring the line properties for each resampled spectrum we obtained $P(\Lambda|\Theta, d_{\rm line})$. This distribution is well approximated by a Gaussian of which we evaluated the dispersion $\sigma_{P(\Lambda|\Theta,d_{\rm line})}$. After checking that the dispersion does not depend strongly on the choice of the subtracted continuum ($\sigma_{P(\Lambda|\Theta,d_{\rm line})} \simeq \sigma_{P(\Lambda|d_{\rm line})} \simeq {\rm constant} \equiv \sigma_\Lambda$) we obtained our line parameter pdf ($P(\Lambda|d_{\rm line})$) by convolving $P_\delta(\Lambda|d_{\rm line})$ with a Gaussian distribution having dispersion equal to σ_Λ. This is equivalent to substituting the $\delta(\Lambda - \Lambda_{\rm best-fit}(\Theta))$ in Equation (12) with $N(\mu = \Lambda_{\rm best-fit}(\Theta), \sigma_\Lambda^2)$.

From this final pdf we estimated the confidence level of each line property as the interval in which the cumulative pdf goes from 16% to 84% (the central 68% credible interval, equivalent to a 1σ confidence level for a Gaussian pdf).

4. RESULTS

4.1. Quasar Continuum Modeling

The "best-fit" continuum models are shown in Figure 2 (red solid lines). In Figure 3 we show the "best-fit" continuum components obtained for J1120+0641 as an example of spectral
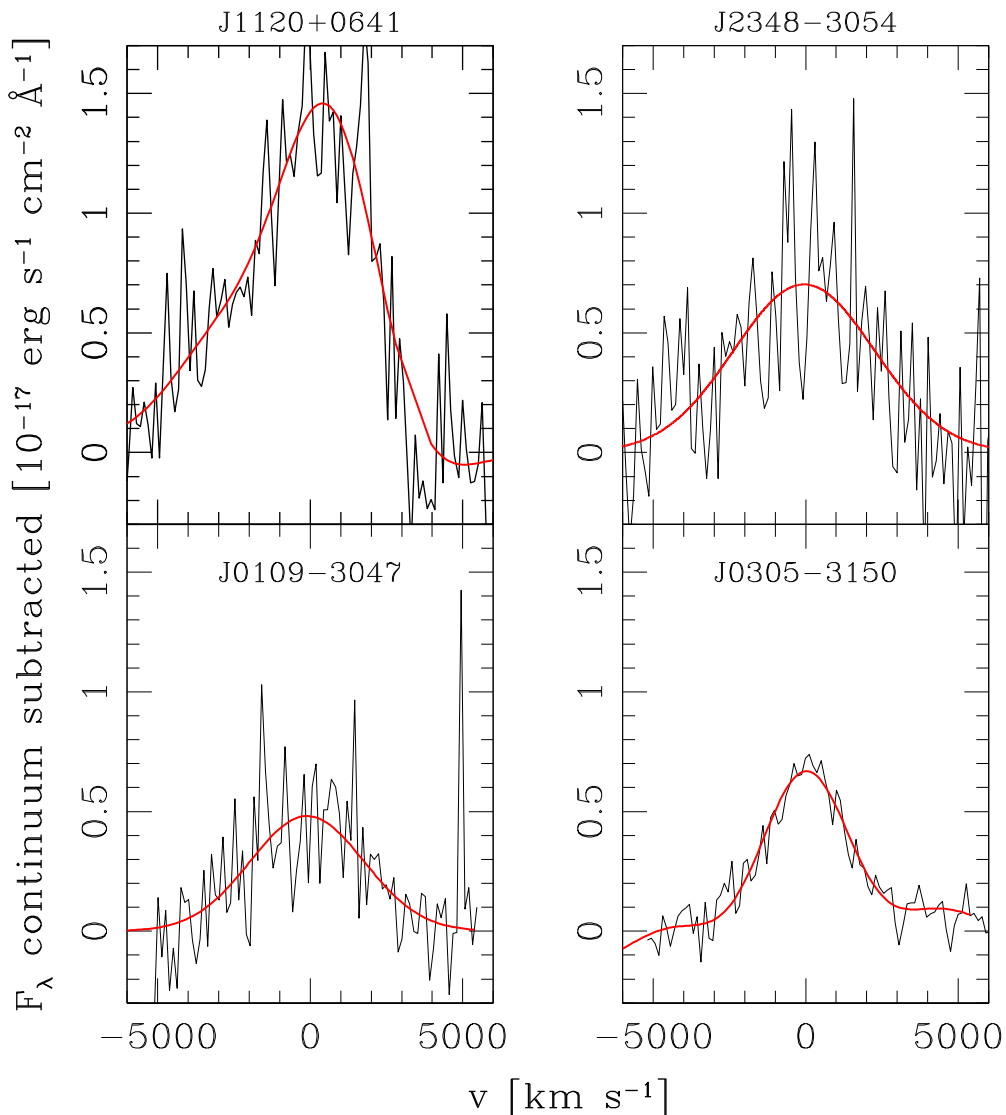
Figure 4. Black solid line: rest-frame flux density in the Mg II fitting window after subtraction of the "best-fit" continuum model. The spectra have been redshifted to the rest-frame system of reference by using the source nominal redshift ($z_{J1120} = 7.084$, $z_{J2348} = 6.89$, $z_{J0109} = 6.75$, $z_{J0305} = 6.606$). Red solid line: "best-fit" emission-line model.

(A color version of this figure is available in the online journal.)

decomposition. Given the individual shapes of the power-law continuum and of the Balmer continuum in the spectral range of interest, the results for the contributions of these two components are expected to be strongly correlated. Therefore it is important to simultaneously model all the pseudo continuum components in order to properly account for degeneracies. In Table 2 we list the best-fit estimates of the power-law slope parameter together with the values corresponding to the 1σ confidence level. The slope coefficients are in agreement within 1σ with both the local slope estimated by De Rosa et al. (2011) and the global value obtained by Decarli et al. (2010).

We estimated the uncertainties on the individual parameters by using the corresponding marginal pdfs. While for J1120+0641 the marginal pdfs for the continuum parameters are regular and show clear individual peaks, for the VIKING quasars we observe very low (if any) contribution of the Balmer continuum. This implies that the Balmer continuum model is not well constrained. Moreover, for J0109–3047 we cannot exclude a zero contribution of the iron component to the continuum model (see Section 4.4.3 for a more detailed discussion).

We point out that, since for the VIKING quasars we were not able to properly cross-check the goodness of the flux calibration and to compute appropriate flux calibration corrections (see Section 2.2), continuum decomposition results hold valid as long as the global spectral shape is preserved.

4.2. Emission-line Modeling and Redshift Estimates

We modeled all the strong UV emission lines detected in the spectrum of J1120+0641: Si IV, C IV, C III], and Mg II. Given the systemic redshift of J0109–3047 and J0305–3150, it was not possible to model their C III] emission line due to telluric contamination. Finally, for J2348–3054, we fully modeled only the Mg II emission line since both Si IV and C IV emission lines are severely affected by absorption (this source is a BAL quasar). Emission-line models obtained after the subtraction of the "best-fit" continuum model are shown in Figures 4 and 5. For each line, we estimated the redshift as

$$z_{line} + 1 = \frac{\lambda_{0,line}}{\mu_{line}}, \qquad (13)$$
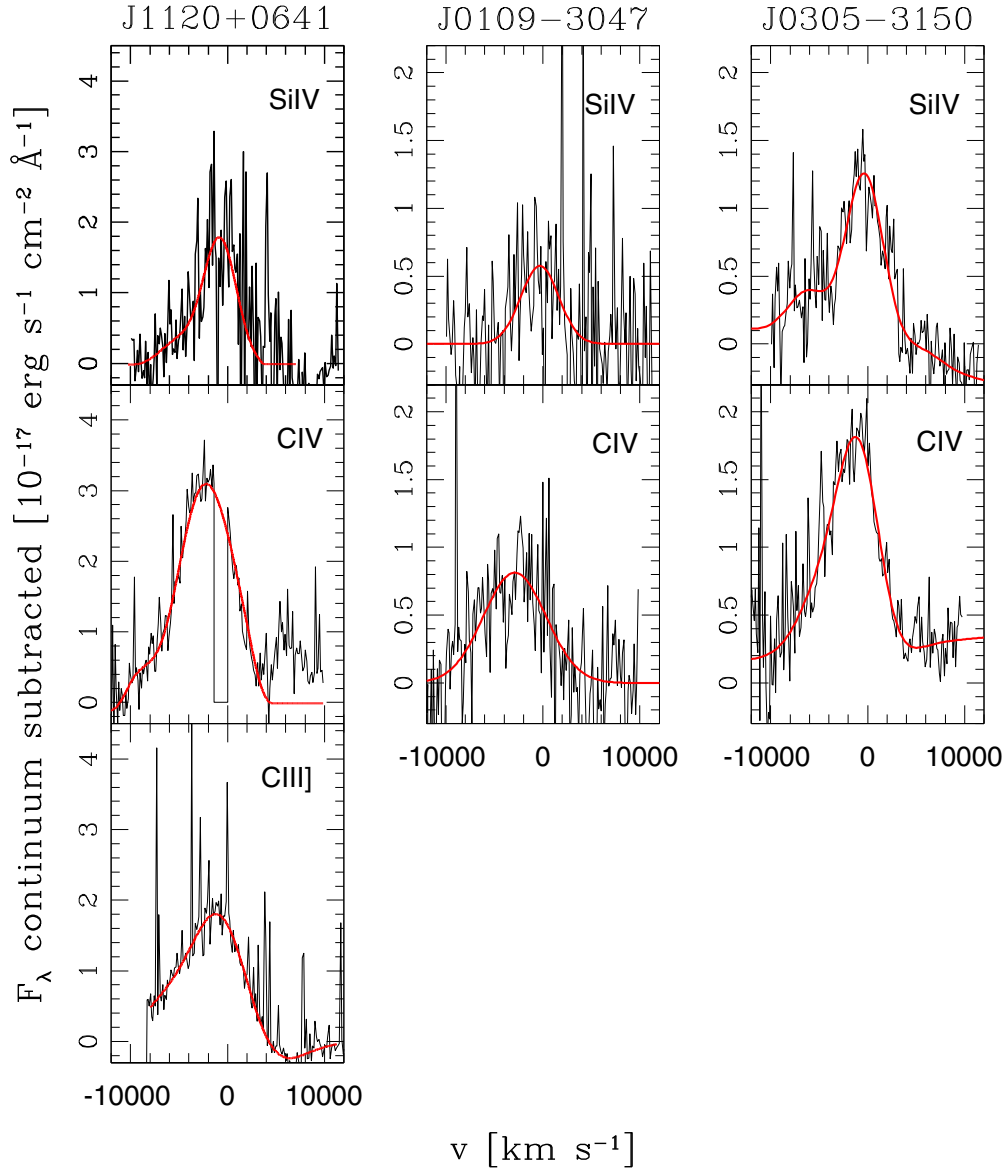
Figure 5. Si IV, C III], and C IV emission lines. Given the systemic redshift of J0109–3047 and J0305–3150, it was not possible to model their C III] emission line due to telluric contamination. The spectra have been redshifted to the rest-frame system of reference by using the source nominal redshift ($z_{J1120} = 7.084$, $z_{J0109} = 6.75$, $z_{J0305} = 6.606$). Black solid line: rest-frame flux density after subtraction of the "best-fit" continuum model. Red solid line: "best-fit" emission-line model. Note that for both J1120+0641 and J0305–3150, Si IV, C III], and C IV are blueshifted with respect to their nominal central wavelengths.

(A color version of this figure is available in the online journal.)

Table 2
Modeled Spectral Properties

	J1120+0641	J2348–3054	J0109–3047	J0305–3150
α	$-1.47^{+0.02}_{-0.01}$	$-2.56^{+0.51}_{-0.63}$	$-1.33^{+0.22}_{-0.07}$	$-1.37^{+0.01}_{-0.01}$
$z_{Mg\,II}$	$7.097^{+0.002}_{-0.001}$	$6.889^{+0.007}_{-0.006}$	$6.747^{+0.007}_{-0.005}$	$6.605^{+0.002}_{-0.001}$
$z_{Si\,IV}$	$7.068^{+0.002}_{-0.003}$	$\cdots$	$6.732^{+0.013}_{-0.010}$	$6.595^{+0.002}_{-0.002}$
$z_{C\,IV}$	$7.024^{+0.001}_{-0.001}$	$\cdots$	$6.675^{+0.006}_{-0.002}$	$6.573^{+0.001}_{-0.004}$
$z_{C\,III]}$	$7.0387^{+0.0007}_{-0.0007}$	$\cdots$	$\cdots$	$\cdots$
$\lambda L_\lambda(1350\,\text{Å})$ (10^{46} erg s^{-1})	4.20 ± 0.02	$\cdots$	1.39 ± 0.06	2.22 ± 0.02
$\sigma_{C\,IV}$ (Å)	$14.72^{+0.15}_{-0.17}$	$\cdots$	$16.5^{+1.1}_{-2.5}$	$18.63^{+0.23}_{-0.62}$
$\lambda L_\lambda(3000\,\text{Å})$ (10^{46} erg s^{-1})	2.90 ± 0.03	0.94 ± 0.33	1.07 ± 0.14	1.66 ± 0.02
FWHM$_{Mg\,II}$ (km s^{-1})	4411^{+210}_{-150}	5446^{+580}_{-360}	4389^{+400}_{-360}	3189^{+110}_{-60}
$F_{Si\,IV}$ (10^{-17} erg s^{-1} cm^{-2})	$41.30^{+0.15}_{-0.17}$	$\cdots$	$13.1^{+6.2}_{-3.8}$	$37.4^{+0.9}_{-1.4}$
$F_{C\,IV}$ (10^{-17} erg s^{-1} cm^{-2})	$117.0^{+1.2}_{-0.8}$	$\cdots$	$33.9^{+6.4}_{-3.2}$	$72.4^{+1.1}_{-1.4}$
$F_{C\,III}$ (10^{-17} erg s^{-1} cm^{-2})	$85.6^{+0.7}_{-0.7}$	$\cdots$	$\cdots$	$\cdots$

where $\lambda_{0,\text{line}}$ is the wavelength of the line peak measured in the observed frame and μ_{line} is the reference laboratory wavelength for the line transition. In Table 2 we list the obtained redshifts while in Figure 6 we show, as an example, the marginal probability distributions for the Mg II line.

For J1120+0641, the $z_{\text{Mg II}}$ estimate and the systemic redshift obtained from molecular gas (Venemans et al. 2012) disagree by more than 3σ, suggesting a redshift of the Mg II low ionization line. On the other hand, the Si IV, C IV, and C III] emission lines for this source present significant blueshifts with respect to the source systemic redshift. Analogously, for J0305–3150, both Si IV and C IV emission lines are significantly blueshifted with respect to the Mg II emission line, that we adopt as a proxy for the systemic redshift (see Section 3.2). However, we need to stress that our estimates of the blueshifts for the Si IV and C III] emission lines might be partially affected by the fact that, given the S/N of our spectra, we model these systems as individual transitions, ignoring the blended components (see Section 3.1.2). It is also worth noticing that the error estimates we cite do not include systematic uncertainties, such as the choice of the line-fitting intervals. For example, for the C IV emission line of J1120+0641, small differences in the choice of the wavelengths excluded from the modeling due to the strong absorption feature affecting the line peak (see Figure 5, left column, central panel), can cause the redshift to vary up to $\Delta z \sim 0.01$ ($\Delta v \sim 350\,\text{km s}^{-1}$).

For both J1120+0641 and J0305–3150, the C IV emission line presents the largest blue-shifts with $\Delta v_{\text{J1120+0641}} = 2260 \pm 40\,\text{km s}^{-1}$ and $\Delta v_{\text{J0305-3150}} = 1300 \pm 150\,\text{km s}^{-1}$. For the C IV emission line in J1120+0641, Mortlock et al. (2011) measured a blue-shift of $\Delta v = 2800 \pm 250\,\text{km s}^{-1}$. While the two estimates seem to disagree by more than 2σ, they should not be directly compared since the emission-line shifts have been estimated in two different ways. We estimated the line redshift starting from the wavelength of the line peak $\lambda_{0,\text{line}}$ (see Equation (13)), while Mortlock et al. (2011) estimated it starting from a flux weighted central wavelength.

4.3. Black Hole Masses

The width of BELs detected in the spectra of active galactic nucleus (AGN) is thought to originate primarily from Doppler broadening related to the motion of the emitting gas around the central BH. Under the assumption that the emitting gas is virialized, M_{BH} can be obtained by combining an estimate of the gas distance from the BH (BLR radius, R_{BLR}) with the velocity of the clouds emitting at R_{BLR} (v_{BLR}),

$$M_{\text{BH}} = f\,G^{-1}\,R_{\text{BLR}}\,v_{\text{BLR}}^2, \qquad (14)$$

where the factor f is a scale factor that depends on inclination, geometry and kinematics of the BLR (e.g., Peterson & Wandel 1999; Decarli et al. 2008; Grier et al 2013) and G is the gravitational constant. The product $G^{-1}\,R_{\text{BLR}}\,v_{\text{BLR}}^2$ includes all the observables, and is often referred to as "virial product." While the gas velocity can be obtained from the width of the BELs, the only way to directly estimate R_{BLR} in non-nearby AGN is through reverberation mapping (RM; e.g., Peterson et al. 2004). RM studies of Hβ emission in local AGNs have lead to the discovery of a tight correlation between the AGN continuum luminosity and the distance of the emitting gas ($R_{\text{BLR}} - L$ relation; Kaspi et al. 2005; Bentz et al. 2009, 2013; Zu et al. 2011). Thanks to this relation, it is possible to estimate the BLR size, and consequently M_{BH}, from single epoch spectra. For
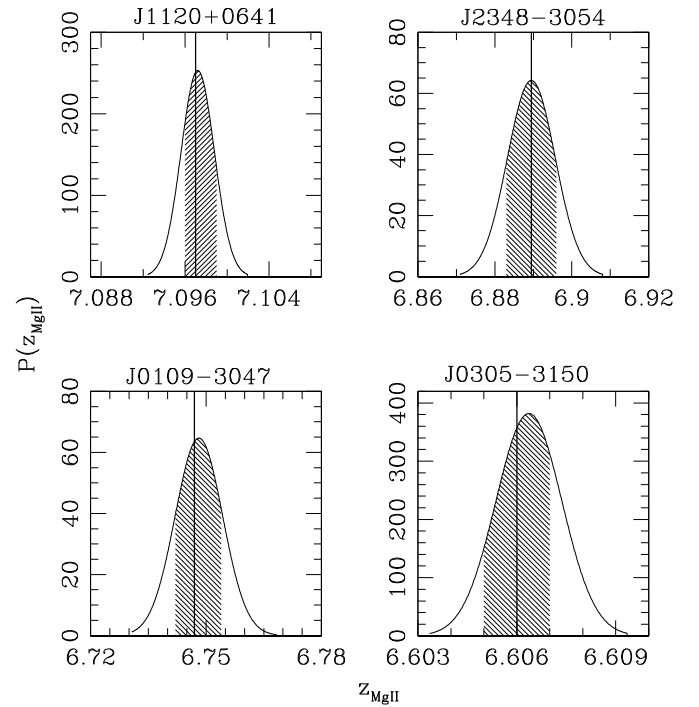

Figure 6. Mg II redshift: marginal probability distributions. The vertical lines indicate the "best-fit" estimate, while the shaded areas correspond to the 1σ confidence level (see Section 3.2 for details).

high-redshift sources, the Hβ emission line is redshifted out of the visible window, and M_{BH} estimates are then based on the C IV and Mg II emission line. For mass estimates based on C IV we used the empirical M_{BH} calibration obtained by Vestergaard & Peterson (2006)

$$M_{\text{BH}}(\text{C IV}) = 10^{6.73} \left(\frac{\sigma_{\text{line}}}{10^3\,\text{km s}^{-1}} \right)^2 \left(\frac{\lambda L_\lambda (1350\,\text{Å})}{10^{44}\,\text{erg s}^{-1}} \right)^{0.53} M_\odot,$$

$$(15)$$

where σ_{line} is the C IV line dispersion and $\lambda L_\lambda (1350\,\text{Å})$ is the monochromatic AGN continuum luminosity estimated at $\lambda_{\text{rest}} = 1350\,\text{Å}$ (see Table 2). For mass estimates based on Mg II instead, we used the empirical calibration obtained by Vestergaard & Osmer (2009)

$$M_{\text{BH}}(\text{Mg II}) = 10^{6.86} \left(\frac{\text{FWHM}_{\text{line}}}{10^3\,\text{km s}^{-1}} \right)^2 \left(\frac{\lambda L_\lambda (3000\,\text{Å})}{10^{44}\,\text{erg s}^{-1}} \right)^{0.5} M_\odot,$$

$$(16)$$

where $\text{FWHM}_{\text{line}}$ is the Mg II line FWHM and $\lambda L_\lambda (3000\,\text{Å})$ is the monochromatic AGN continuum luminosity estimated at $\lambda_{\text{rest}} = 3000\,\text{Å}$ (see Table 2). Both relations were calibrated to the Peterson et al. (2004) RM results, and are consistent within ~ 0.1 dex (Vestergaard & Osmer 2009). The 1σ scatter in the absolute zero points are equal to 0.32 dex for the C IV relation and to 0.55 dex for the Mg II relation. The intrinsic scatter of the estimators dominates the M_{BH} measurement uncertainties. For the C IV emission line we opted to estimate the gas velocity from the line dispersion instead of the line FWHM, following Denney et al. (2013).

In Table 3 we list the M_{BH} estimates obtained from the Mg II emission line, while in Figure 7 we show the corresponding marginal pdfs. The uncertainties we report do not include the systematic uncertainties intrinsic to the M_{BH} estimators. The
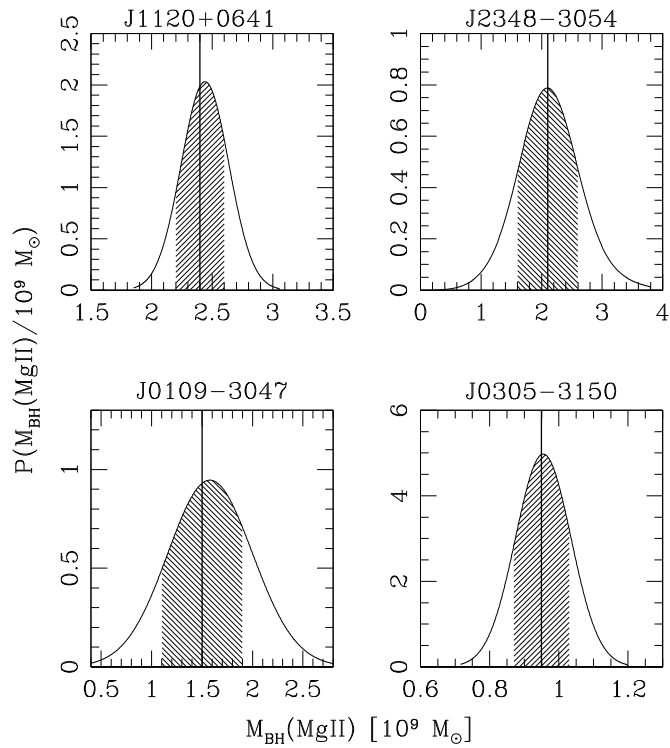
Figure 7. M_{BH} estimates from Mg II emission line: marginal probability distributions. The vertical lines indicate the "best-fit" estimate, while the shaded areas correspond to the 1σ confidence level (see Section 3.2 for details).

M_{BH} estimate for J1120+0641 agrees within 1σ with the value obtained by Mortlock et al. (2011) ($M_{BH} = 2.0^{+1.5}_{-0.7} \times 10^9 \, M_\odot$).

For J1120+0641, J0109–3047, and J0305–3150, we were able to estimate the M_{BH} from the C IV emission line (see Table 3). Even in cases where (1) the C IV emission line presents extreme blueshifts (e.g., for J1120+0641, $\Delta v \geqslant 2000 \, \mathrm{km \, s^{-1}}$); (2) the C IV emission-line profile is affected by absorption (e.g., the C IV line of J1120+0641 presents an absorption doublet close to the line peak, see Figure 5 central left panel); and (3) the spectrum is characterized by low S/N (e.g., J0109–3047, see Figure 5 central panel), we are able to recover the M_{BH} within a factor of two. If we consider the scatter in the zero point of the two estimators, the M_{BH} obtained from the Mg II and C IV lines are in agreement within 1σ.

We further computed the quasar Eddington ratios defined as the ratio between the AGN bolometric luminosity L_{Bol} and the theoretical Eddington luminosity L_{Edd}. The AGN bolometric luminosity was obtained by applying the bolometric correction computed by Shen et al. (2008) to the observed monochromatic luminosity $\lambda L_\lambda(3000 \, \text{Å})$,

$$L_{Bol} = 5.15 \, \lambda L_\lambda(3000 \, \text{Å}). \qquad (17)$$

The Eddington luminosity is defined as the maximum luminosity attainable at which the radiation pressure acting on the gas counterbalances the gravitational attraction of the BH,

$$L_{Edd} = 1.3 \times 10^{38} \left(\frac{M_{BH}}{M_\odot} \right) \text{erg s}^{-1}. \qquad (18)$$

We computed L_{Edd} from M_{BH} (Mg II). Since different M_{BH} estimators can lead to significant differences in the M_{BH} estimates, and we aim to compare the Eddington ratios of the $z > 6.5$ quasars to the Eddington ratio distribution of the

Table 3
Estimated M_{BH}, Quasar Eddington Ratios, Emission Line Ratios, and C IV EW

	J1120+0641	J2348–3054	J0109–3047	J0305–3150
M_{BH} (Mg II) ($10^9 \, M_\odot$)	$2.4^{+0.2}_{-0.2}$	$2.1^{+0.5}_{-0.5}$	$1.5^{+0.4}_{-0.4}$	$0.95^{+0.08}_{-0.07}$
M_{BH} (C IV) ($10^9 \, M_\odot$)	$1.09^{+0.02}_{-0.04}$	$\cdots$	$0.77^{+0.05}_{-0.1}$	$1.20^{+0.06}_{-0.05}$
L_{Bol}/L_{Edd}	0.48	0.18	0.24	0.68
$L_{Bol}/L_{Edd\,2011}$	0.52	0.19	0.26	0.74
Si IV/C IV	0.35 ± 0.01	$\cdots$	0.39 ± 0.19	0.52 ± 0.02
C III]/C IV	0.73 ± 0.01	$\cdots$	$\cdots$	$\cdots$
Fe II/Mg II	$2.10^{+0.13}_{-0.02}$	$2.8^{+0.3}_{-1.0}$	$1.8^{+2.5}_{-1.8}$	$3.2^{+0.7}_{-0.7}$
EW$_{C\,IV}$ (Å)	26.3 ± 0.3	$\cdots$	$20.6 \pm +4.7$	27.0 ± 0.8

Notes. $L_{Bol}/L_{Edd\,2011}$ is obtained by using Equation (4) of De Rosa et al. (2011).

$4.0 < z < 6.5$ quasars obtained by De Rosa et al. (2011), we also re-computed M_{BH} (Mg II) using the same M_{BH} estimator as De Rosa et al. (2011). In Table 3 we list L_{Bol}/L_{Edd}, and the comparison values obtained by estimating M_{BH} through Equation (4) of De Rosa et al. (2011). The L_{Bol}/L_{Edd} values obtained through the two estimators are in excellent agreement. The $z > 6.5$ quasars are characterized by an average Eddington ratio of $\langle \log(L_{Bol}/L_{Edd}) \rangle = -0.4 \pm 0.2$, which is in agreement within 1σ with the average Eddington ratio obtained for the $4.0 < z < 6.5$ sample: $\langle \log(L_{Bol}/L_{Edd}) \rangle = -0.3 \pm 0.3$.

M_{BH} estimates and relative Eddington ratios of high-redshift quasars can be used to give constraints on the formation processes of SMBHs in the early universe. The time needed by a BH seed to grow at a constant rate from an initial mass M_0 to a final mass M_t is equal to (Shapiro 2005)

$$t = 0.45 \, \text{Gyr} \left(\frac{\epsilon}{1 - \epsilon} \right) \frac{L_{Edd}}{L_{Bol}} \ln \left(\frac{M_t}{M_0} \right), \qquad (19)$$

where 0.45 Gyr is the is the characteristic accretion timescale (obtained assuming a mean molecular weight per electron $\mu_e = 1$), ϵ is the radiative efficiency ($\epsilon \sim 0.07$, Volonteri & Rees 2005), and L_{Bol}/L_{Edd} is the Eddington ratio. A BH seed with mass equal to $M_0 = (1–6) \times 10^2 \, M_\odot$, which is the hypothesized mass of a BH seed originated by a Pop III star (see Volonteri 2010, for a review on SMBH formation), accreting constantly at an Eddington ratio of ~0.4 (equal to the average Eddington ratio of our $z > 6.5$ sample) would need ~1.2–1.4 Gyr to grow up to $M_{BH} = 10^9 \, M_\odot$. However, at the redshift characteristic of our sources $z = 6.5$–7.1, the universe is only ~0.8 Gyr old while the BHs powering the quasars have already $M_{BH} \gtrsim 10^9 \, M_\odot$. If we invert Equation (19), and we assume that the BH seeds grew up to $M_t \sim 10^9 \, M_\odot$ at a constant Eddington ratio of ~0.4 from $z_0 = 10, 15, \infty$ (accretion time $t \sim 0.3, 0.5, 0.8 \, \text{Gyr}$), we find that the BH seed needs to have a mass of $M_0 \sim 3 \times 10^7, 3 \times 10^6, 8 \times 10^4 \, M_\odot$ respectively. Although this is suggesting that highly massive BH ($M_0 \gtrsim 10^4 \, M_\odot$) seeds are needed at early times ($z \gtrsim 20$–30) in order to observe $M_t \sim 10^9 \, M_\odot$ at $z = 6.5$–7.1, it is extremely difficult to put robust constraints on the seed masses. These results are in fact highly dependent on the adopted Eddington ratio, which, in turn, is a function of the M_{BH} estimate (characterized by a systematic uncertainty of ~2). For example, using the same assumption as above, if $L_{Bol}/L_{Edd} = 0.1$ we obtain $M_0 \sim 4 \times 10^8, 2 \times 10^8, 9 \times 10^7 \, M_\odot$, while for $L_{Bol}/L_{Edd} = 1$ we obtain $M_0 \sim 1 \times 10^5, 4 \times 10^2, 1 \times 10^{-2} \, M_\odot$.
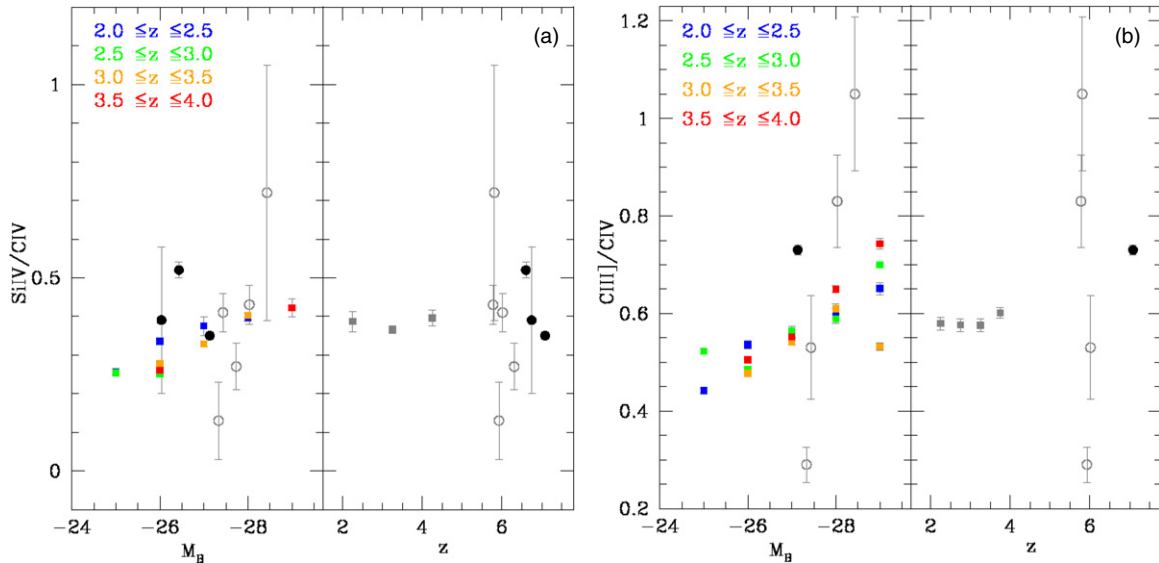
Figure 8. Si IV/C IV (a) and C III]/C IV (b) flux ratios. Left panels: flux ratios as a function of the quasar brightness. Colored squares: flux ratios measured in the composite spectra of lower-redshift quasars, Nagao et al. (2006); the color coding represents the redshift bins (blue: $2.0 \leqslant z \leqslant 2.5$; green: $2.5 \leqslant z \leqslant 3.0$; orange: $3.0 \leqslant z \leqslant 3.5$; red: $3.5 \leqslant z \leqslant 4.0$). Gray empty circles: $z \sim 6$ quasars, Jiang et al. (2007). Black filled circles: $z > 6.5$ sample. Right panels: flux ratios evolution as a function of redshift. Gray squares: flux ratios measured in the composite spectra of quasars in the luminosity range $-28.5 < M_B < -26.5$, Nagao et al. (2006). Gray circles: $z \sim 6$ quasars, Jiang et al. (2007). Black filled circles: $z > 6.5$ sample.

(A color version of this figure is available in the online journal.)

4.4. Emission-line Properties

4.4.1. Si IV/C IV and C III]/C IV Line Ratios

As we discussed in Section 1, emission-line ratios can be used to study the BLR chemical enrichment and track its evolution with redshift. It has been shown that the abundance of nitrogen (N) relative to carbon, oxygen, and helium (C, O, and He) can be used as a crude marker of the degree of chemical enrichment of the BLR (e.g., Hamann et al. 2002). This is due to the fact that N is a second generation element, i.e., slowly produced in stars from previously synthesized C and O. In particular, Hamann et al. (2002) showed that the most robust abundance probes are N III]/O III], N V/(C IV+O IV), and N V/He II. Even though the typical S/N of our current spectra, together with the severe systematics affecting the Lyα complex, does not allow us to estimate the BLR metallicity through N V/(C IV+O IV) and N V/He II flux ratios, the study of the BEL flux ratios as a function of look-back time does in itself carry significant information about the BLR chemical enrichment history. Nagao et al. (2006) analyzed a sample of 5000 quasars from the SDSS Second Data Release: they built quasar composite spectra in the ranges of $2 \leqslant z \leqslant 4.5$ and $-29.5 \leqslant M_B \leqslant -24.5$ mag and measured the emission-line ratios in the composite spectra for each redshift and luminosity bin. They found that while there are significant correlations between most of the line ratios and the quasars luminosities, the flux ratios do not show strong evolution with redshift. The latter result was further confirmed by Jiang et al. (2007).

We were able to estimate the Si IV/C IV flux ratio for J1120+0641, J0109–3047, and J0305–3150, and the C III]/C IV flux ratio for J1120+0641 (we list the emission-line fluxes in Table 2, while flux ratios are listed in Table 3). In Figure 8 we show the emission-line flux ratios (Figure 8(a): Si IV/C IV; Figure 8(b): C III]/C IV) obtained for the $z > 6.5$ sample as a function of quasar luminosity (left panel) and redshift (right panel). Together with the results for our sample we plot the flux ratios of five $z \sim 6$ quasars obtained by Jiang

et al. (2007), and the flux ratios measured in the composite spectra of $2 \leqslant z \leqslant 4.5$ quasars by Nagao et al. (2006). In Figure 8 left panels (flux ratios as a function of luminosity) we plot the results for the lower-redshift sample color-coded as a function of redshift, while in the right panels (flux ratios as a function of redshift) we plot only the flux ratios obtained for a sub-sample of lower-redshift quasars with luminosity comparable to the $z \sim 6$–7 objects ($-28.5 \leqslant M_B \leqslant -26.5$ mag). For the high-redshift quasars, M_B was obtained by applying to the respective M_{1450} (Jiang et al. 2006; Mortlock et al. 2011; Venemans et al. 2013) a color conversion factor that was computed from the SDSS quasar composite spectrum (Vanden Berk et al. 2001). It is important to notice that while we are modeling Si IV +O IV] and C III] +Al III+Si III] as individual transitions (see Section 3.1.2), Nagao et al. (2006) were able to decompose these emission-line complexes and model their individual components. At the same time, Jiang et al. (2007) modeled the Al III line in four $z \sim 6$ quasars. In cases were a decomposition was performed, we plot the flux corresponding to the entire emission-line complex, obtained as the sum of the flux of the individual components.

There is no evidence of evolution of the Si IV/C IV flux ratio in the $2.0 \leqslant z \leqslant 7.1$ redshift range (see Figure 8(a)). For the C III]/C IV line ratio the situation is more controversial. At a given luminosity, high-redshift sources can present flux ratios that are a factor ~two different than the ones characteristic of the lower-redshift sample. If we consider the luminosity-matched sub-sample (see Figure 8(b), right panel), the C III]/C IV line ratio does not show any significant evolution up to $z \sim 4$ ($<C III]/C IV > = 0.58 \pm 0.01$). For the $z \sim 6$–7 objects instead, we find significant scatter in the measured line ratios ($0.2 \leqslant C III]/C IV \leqslant 1.2$). In particular, at $z = 7.1$ C III]/C IV $= 0.57$, which is ~1.3 times higher than the typical ratio of the luminosity-matched lower-redshift sample. However, given the low number of sources at $z \geqslant 4$, we cannot draw any definitive conclusion about a possible dependence of the C III]/C IV on redshift.
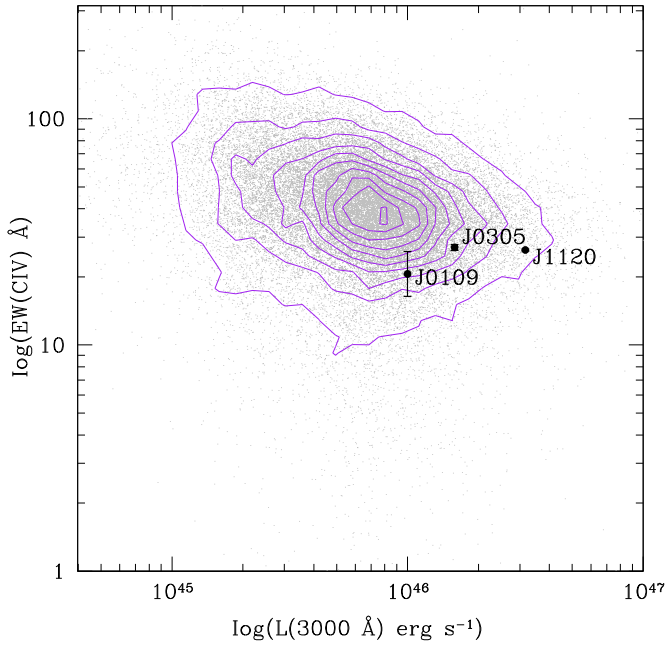
Figure 9. C IV EW as a function of the AGN continuum luminosity. Black point: the $z > 6.5$ quasars. Gray dots: $1.5 \leqslant z \leqslant 2.25$ quasars from the SDSS Data Release 7, Shen et al. (2011). The $z > 6.5$ quasars are in agreement with the trend observed for the lower-redshift sample.

(A color version of this figure is available in the online journal.)

4.4.2. C IV Equivalent Width

The EWs of high ionization lines anti-correlate with the underlying AGN continuum luminosity. The observed degree of anti-correlation is a function of the line ionization potential (the higher the line ionization potential, the stronger is the anti-correlation Baldwin et al. 1989; Netzer et al. 1992). This relation, also known as Baldwin effect, was first detected for the C IV emission line by Baldwin (1977) in a sample of nearby quasars.

We were able to measure the C IV EW for all the sources in our sample but J2348–3054, since it is a BAL quasar. The resulting C IV EWs are listed in Table 3. In Figure 9 we plot the C IV EW as a function of the AGN continuum luminosity. Together with the $z > 6.5$ quasars (black points) we are plotting the results for a sample of 36000 quasars with $1.5 \leqslant z \leqslant 2.25$ from the SDSS Data Release 7 (grey dots, purple contours; Shen et al. 2011). The $z > 6.5$ quasars are in agreement with the trend observed for the lower-redshift sample.

4.4.3. Fe II/Mg II Line Ratio

As discussed in Section 1 the abundance of Fe and Mg is of particular interest for understanding the chemical evolution of galaxies at high-z. We computed the Fe II flux by integrating the normalized Fe II template over the rest-frame wavelength range 2200 Å $< \lambda_{\rm rest} < 3090$ Å. In Table 3, we list the Fe II/Mg II line ratios obtained, while in Figure 10 we show the marginal pdfs. The uncertainties we report do not include systematic uncertainties. The resulting pdfs are dominated by the marginal pdf of the normalization of the Fe II template, and are significantly broader for the spectra with continuum S/N $\lesssim 10$ (J2348–3054 and J0109–3047). At low S/N in fact, features such as the Fe II complexes, that are significantly fainter than the bright BELs, become more difficult to detect and, consequently, the Fe II template normalization becomes less
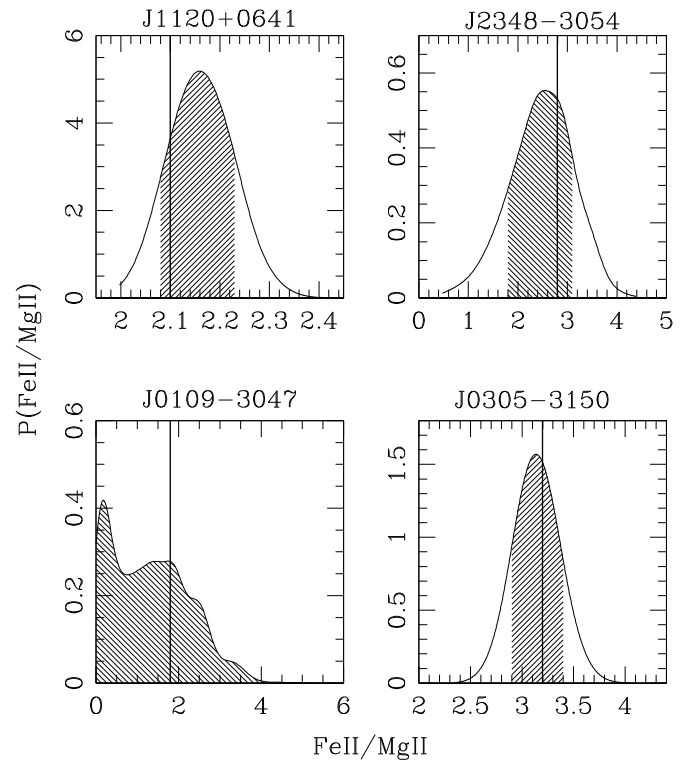

Figure 10. Fe II/Mg II flux ratios: marginal probability distributions. The vertical lines indicate the "best-fit" estimate, while the shaded areas correspond to the 1σ confidence level for J1120+0641, J2348–3054, and J0305–3150, and to the 3σ confidence level for J0109–3047 (see Section 3.2 for details).

constrained. In particular, for J0109–3047, the Fe II/Mg II ratio is highly unconstrained: $0 \leqslant$Fe II/Mg II $\leqslant 4.3$ with 99.73% probability (corresponding to a 3σ confidence level).

In Figure 11 we show the evolution of the Fe II/Mg II line ratio as function of redshift. Together with the $z > 6.5$ sample we plot the Fe II/Mg II flux ratios obtained by De Rosa et al. (2011) for a sample of 22 sources with $4.0 < z < 6.4$. Even if we are extending the probed redshift range up to $z \sim 7$ (when the age of the universe is ~ 0.8 Gyr), we still do not see any evidence for evolution of the Fe II/Mg II line ratio as a function of cosmic time.

In a previous study (De Rosa et al. 2011) we found that the Fe II/Mg II line ratio measurements are significantly dependent on the adopted modeling procedure. Therefore, we performed an additional fit of the spectral continuum after adapting our procedure to the one followed by De Rosa et al. (2011), where we considered a sub-class of continuum models with respect to the ones considered in this work:

1. we limited the continuum windows to $2000 \leqslant \lambda_{\rm rest} \leqslant 3000$, in order to consider the same broad Fe II complexes;
2. we considered a single Balmer continuum template with $T_{\rm e} = 15000$ K, and $\tau = 1$; and
3. we fixed the normalization of the Balmer Continuum such that $F_{\rm BC}(3675\,\text{Å}) = 0.3 \times F_{\rm PL}(3675\,\text{Å})$.

All the resulting Fe II/Mg II line ratios are in agreement within 3σ with previous estimates.

To constrain the chemical evolution of the BLR gas in these high-redshift quasars, one would need to connect the measured Fe II/Mg II line ratios with the corresponding Fe/Mg abundance ratios. Unfortunately, an accurate conversion cannot be performed since it has been shown that that the
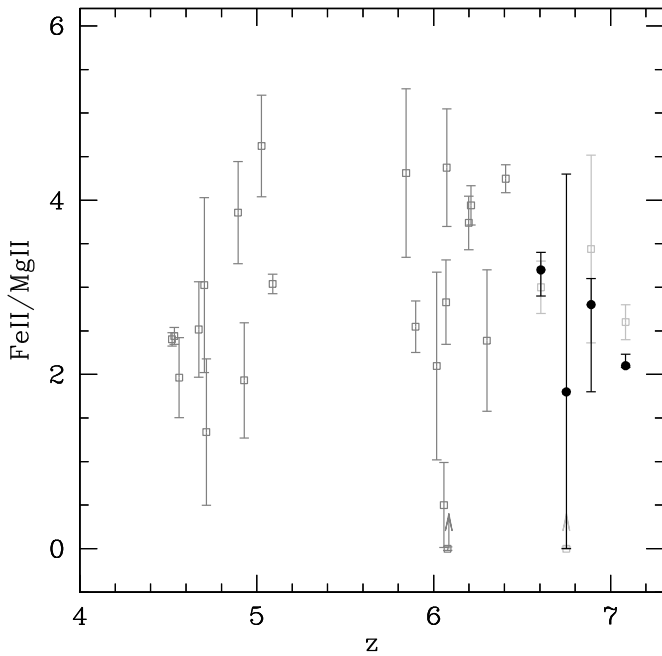
Figure 11. Fe II/Mg II line ratio as a function of redshift for $z > 4$. Black filled circles: $z > 6.5$ sample; for J0109–3047 we are reporting the 3σ confidence level. Dark gray empty squares: $4.0 < z < 6.4$ sample, De Rosa et al. (2011). Light gray empty squares: Fe II/Mg II ratios obtained for the $z > 6.5$ sample using the same continuum model as De Rosa et al. (2011). There is no evidence for evolution of the estimated Fe II/Mg II line ratio as a function of cosmic age for $4.0 < z < 7.1$ in the quasar sample.

Fe II/Mg II ratio is not only sensitive to the corresponding Fe and Mg abundances, but also to the hydrogen density, to the properties of the radiation field and to the gas micro-turbulence (Baldwin et al. 2004; Verner et al. 2003, 2004; Bruhweiler & Verner 2008). Therefore, following De Rosa et al. (2011), we can conclude that the lack of evolution in the Fe II/Mg II can be interpreted as an early enrichment of the quasar host only under the assumption that, in the analyzed sources, the physical conditions that determine the Fe II emission are sufficiently similar. Under such assumption, the quasar hosts must have undergone a major episode of Fe enrichment before the cosmic age at which they have been observed ($\sim$0.8 Gyr). On the other hand, if Fe and Mg are produced respectively via SNe Ia and core collapse supernovae, one would expect Fe to be substantially produced at least 1 Gyr after the initial burst of star formation (e.g., Hamann & Ferland 1993). However, the expected enrichment time and our observations are not in disagreement if we consider that the actual picture is probably more complex. Fe could in fact be generated by Pop III stars: extremely metal poor stars with typical masses $M \gtrsim 100\,M_\odot$ that might be able to produce large amounts of Fe by $z \leqslant 10$ (Heger & Woosley 2002). At the same time, stellar nuclear yields are still rather uncertain, and there are various scenarios in which significant metal production can occur at early enough times to obtain a fully enriched BLR at $z \sim 7$ (Matteucci & Recchi 2001; Venkatesan et al. 2004).

5. SUMMARY

We have analyzed of optical and NIR spectra of the only four $z > 6.5$ quasars known to date: J1120+0641, discovered in the UKIDSS-LAS survey, and J2348–3054, J0109–3047, and J0305–3150, recently discovered in the VISTA-VIKING survey. We presented new deep VLT/X-Shooter observations for J1120+0641. Together with the new data, we analyzed all the

observations of the $z > 6.5$ sources collected by our group using the VLT/X-Shooter spectrograph and the Magellan/FIRE spectrograph. The collected spectra provide essentially simultaneous coverage of the 10000–24000 Å wavelength range. The quality of this data set is likely the best achievable with the currently available facilities.

We used the spectra to estimate the masses of the BHs that are powering these $z > 6.5$ quasars and to study their emission-line properties. The spectra were modeled using a combination of a power-law continuum, a Balmer continuum, an Fe II +Fe III template, and a series of emission lines. We developed a maximum likelihood procedure for the spectral modeling, which allows a reliable estimate of how the uncertainties in the continuum modeling propagate into the estimates of the physical quantities of interest. The $z > 6.5$ quasars are observationally indistinguishable from their counterparts at lower redshifts.

We estimated the $M_{\rm BH}$ from the Mg II and C IV emission lines using empirical mass-scaling relations. The $M_{\rm BH}$ obtained from the two estimators agree within 1σ. The quasars in our sample host BHs with masses of $\sim 10^9\,M_\odot$ that are accreting close to the Eddington luminosity ($\langle \log(L_{\rm Bol}/L_{\rm Edd}) \rangle = -0.4 \pm 0.2$), in agreement with the average Eddington ratio obtained for a $4.0 < z < 6.5$ sample. If the measured average Eddington ratio is representative of the typical quasar accretion rate in the early universe, highly massive BH seeds ($M_0 \gtrsim 10^4\,M_\odot$) need to be in place at very early times ($z \gtrsim 20$–30) in order to be able to observe BHs with $M_{\rm BH} \sim 10^9\,M_\odot$ at $z = 6.5$–7.1. At the same time, quasar accretion episodes characterized by such high rates must be short in time and limited in number. If the BHs powering our sources had been accreting at an Eddington ratio of $\sim$0.4 for one additional characteristic accretion time ($t \sim 0.45\,{\rm Gyr}$), they would have reached masses of $\sim 10^{11}\,M_\odot$, which is one order of magnitude larger than the most massive BH observed in the local universe.

We estimated the Si IV/C IV and C III]/C IV flux ratios and compared them with the results obtained from luminosity matched sub-samples at $z \sim 6$ and $2 \leqslant z \leqslant 4.5$. We find no evidence of evolution of these line ratios with cosmic time.

We calculated fluxes for the Mg II and Fe II lines and compared the measured Fe II/Mg II ratio with the results obtained for a sample of $4.0 < z < 6.4$ quasars. Since the Fe II/Mg II line ratio measurements are significantly dependent on the adopted modeling procedure, we performed a consistent analysis of the two samples. We do not detect any redshift evolution of the Fe II/Mg II ratio for $4.0 < z < 7.1$. If we assume that the Fe II/Mg II line ratio is a reliable proxy of the Fe/Mg abundance ratio, this indicates that the $z > 6.5$ quasar hosts must have undergone a major episode of Fe enrichment in the first $\sim$0.8 Gyr after the Big Bang.

REFERENCES

Arnaboldi, M., Neeser, M. J., Parker, L. C., et al. 2007, Msngr, 127, 28
Assef, R. J., Frank, S., Grier, C. J., et al. 2012, ApJ, 753, 2
Baldwin, J. A. 1977, ApJ, 214, 679
Baldwin, J. A., Ferland, G. J., Korista, K. T., Hamann, F., & LaCluyzé, A. 2004, ApJ, 615, 610

Baldwin, J. A., Wampler, E. J., & Gaskell, C. M. 1989, ApJ, 338, 630
Bañados, E., Venemans, B. P., Morganson, E., et al. 2014, AJ, in press (arXiv:1405.3986)
Barth, A. J., Martini, P., Nelson, C. H., & Ho, L. C. 2003, ApJL, 594, L95
Bentz, M. C., Denney, K. D., Grier, C. J., et al. 2013, ApJ, 767, 149
Bentz, M. C., Walsh, J. L., Barth, A. J., et al. 2009, ApJ, 705, 199
Bolton, J. S., Haehnelt, M. G., Warren, S. J., et al. 2011, MNRAS, 416, L70
Bruhweiler, F., & Verner, E. 2008, ApJ, 675, 83
Cardelli, J. A., Clayton, G. C., & Mathis, J. S. 1989, ApJ, 345, 245
De Rosa, G., Decarli, R., Walter, F., et al. 2011, ApJ, 739, 56
Decarli, R., Falomo, R., Treves, A., et al. 2010, MNRAS, 402, 2453
Decarli, R., Labita, M., Treves, A., & Falomo, R. 2008, MNRAS, 387, 1237
Denney, K. D., De Rosa, G., Croxall, K., et al. 2014, ApJ, submitted (arXiv:1404.4879D)
Denney, K. D., Pogge, R. W., Assef, R. J., et al. 2013, ApJ, 775, 60
Dietrich, M., Hamann, F., Appenzeller, I., & Vestergaard, M. 2003, ApJ, 596, 817
Fan, X., Strauss, M. A., Becker, R. H., et al. 2006, AJ, 131, 1203
Grandi, S. A. 1982, ApJ, 255, 25
Grier, C. J., Martini, P., Watson, L. C., et al. 2013, ApJ, 773, 90
Gunn, J. E., & Peterson, B. A. 1965, ApJ, 142, 1633
Hamann, F., & Ferland, G. 1993, ApJ, 418, 11
Hamann, F., Korista, K. T., Ferland, G. J., Warner, C., & Baldwin, J. 2002, ApJ, 564, 592
Heger, A., & Woosley, S. E. 2002, ApJ, 567, 532
Hewett, P. C., & Wild, V. 2010, MNRAS, 405, 2302
Iwamuro, F., Kimura, M., Eto, S., et al. 2004, ApJ, 614, 69
Jiang, L., Fan, X., Annis, J., et al. 2008, AJ, 135, 1057
Jiang, L., Fan, X., Bian, F., et al. 2009, AJ, 138, 305
Jiang, L., Fan, X., Hines, D. C., et al. 2006, AJ, 132, 2127
Jiang, L., Fan, X., Vestergaard, M., et al. 2007, AJ, 134, 1150
Kaiser, N., Burgett, W., Chambers, K., et al. 2010, Proc. SPIE, 7733, 12
Kaspi, S., Maoz, D., Netzer, H., et al. 2005, ApJ, 629, 61
Komatsu, E., Smith, K. M., Dunkley, J., et al. 2011, ApJS, 192, 18
Kurk, J. D., Walter, F., Fan, X., et al. 2007, ApJ, 669, 32
Kurk, J. D., Walter, F., Fan, X., et al. 2009, ApJ, 702, 833
Latif, M. A., Schleicher, D. R. G., Schmidt, W., & Niemeyer, J. 2013, MNRAS, 433, 1607
Lawrence, A., Warren, S. J., Almaini, O., et al. 2007, MNRAS, 379, 1599
Matteucci, F., & Greggio, L. 1986, A&A, 154, 279
Matteucci, F., & Recchi, S. 2001, ApJ, 558, 351
Modigliani, A., Goldoni, P., Royer, F., et al. 2010, Proc. SPIE, 7737, 773728
Morganson, E., De Rosa, G., Decarli, R., et al. 2012, AJ, 143, 142
Mortlock, D. J., Warren, S. J., Venemans, B. P., et al. 2011, Natur, 474, 616
Nagao, T., Maiolino, R., & Marconi, A. 2006, A&A, 447, 157

Netzer, H., Laor, A., & Gondhalekar, P. M. 1992, MNRAS, 254, 15
Peterson, B. M., Ferrarese, L., Gilbert, K. M., et al. 2004, ApJ, 613, 682
Peterson, B. M., & Wandel, A. 1999, ApJ, 521, 95
Pipino, A., Fan, X. L., Matteucci, F., et al. 2011, A&A, 525, 61
Richards, G. T., Kruczek, N. E., Gallagher, S. C., et al. 2011, AJ, 141, 167
Richards, G. T., Vanden Berk, D. E., Reichard, T. A., et al. 2002, AJ, 124, 1
Riffel, R. A. 2010, Ap&SS, 327, 239
Schlegel, D. J., Finkbeiner, D. P., & Davis, M. 1998, ApJ, 500, 525
Shang, Z., Wills, B. J., Wills, D., & Brotherton, M. S. 2007, AJ, 134, 294
Shapiro, S. L. 2005, ApJ, 620, 59
Shen, Y., Greene, J. E., Strauss, M. A., Richards, G. T., & Schneider, D. P. 2008, ApJ, 680, 169
Shen, Y., Richards, G. T., Strauss, M. A., et al. 2011, ApJS, 194, 45
Simcoe, R. A., Burgasser, A. J., Schechter, P. L., et al. 2013, PASP, 125, 270
Simcoe, R. A., Cooksey, K. L., Matejek, M., et al. 2011, ApJ, 743, 21
Simcoe, R. A., Sullivan, P. W., Cooksey, K. L., et al. 2012, Natur, 492, 79
Tinsley, B. M. 1979, ApJ, 229, 1046
Trakhtenbrot, B., Netzer, H., Lira, P., & Shemmer, O. 2011, ApJ, 730, 7
Vanden Berk, D. E., Richards, G. T., Bauer, A., et al. 2001, AJ, 122, 549
van der Marel, R. P., & Franx, M. 1993, ApJ, 407, 525
Venemans, B. P., Findlay, J. R., Sutherland, W. J., et al. 2013, ApJ, 779, 24
Venemans, B. P., McMahon, R. G., Walter, F., et al. 2012, ApJL, 751, L25
Venemans, B. P., McMahon, R. G., Warren, S. J., et al. 2007, MNRAS, 376, 76
Venkatesan, A., Schneider, R., & Ferrara, A. 2004, MNRAS, 349, 43
Verner, E., Bruhweiler, F., Verner, D., Johansson, S., & Gull, T. 2003, ApJ, 592, 59
Verner, E., Bruhweiler, F., Verner, D., et al. 2004, ApJ, 611, 780
Vernet, J., Dekker, H., D'Odorico, S., et al. 2011, A&A, 536, A105
Vestergaard, M., & Osmer, P. S. 2009, ApJ, 699, 800
Vestergaard, M., & Peterson, B. M. 2006, ApJ, 641, 689
Vestergaard, M., & Wilkes, B. J. 2001, ApJS, 134, 1
Volonteri, M. 2010, A&AR, 18, 279
Volonteri, M., & Rees, M. J. 2005, ApJ, 633, 624
Walter, F., Bertoldi, F., Carilli, C., et al. 2003, Natur, 424, 406
Walter, F., Riechers, D. A., Cox, P., et al. 2009, Natur, 457, 699
Wang, R., Carilli, C. L., Neri, R., et al. 2010, ApJ, 714, 699
Wang, R., Wagg, J., Carilli, C. L., et al. 2013, ApJ, 773, 44
Willott, C. J., Delorme, P., Omont, A., et al. 2007, AJ, 134, 2435
Willott, C. J., Delorme, P., Reylé, C., et al. 2010, AJ, 139, 906
Wills, B. J., Netzer, H., & Wills, D. 1985, ApJ, 288, 94
York, D. G., Adelman, J., Anderson, J. E., Jr., et al. 2000, AJ, 120, 1579
Yoshii, Y., Tsujimoto, T., & Nomoto, K. 1996, ApJ, 462, 266
Zu, Y., Kochanek, C. S., & Peterson, B. M. 2011, ApJ, 735, 80